Frequency-Domain Gust Response Simulation using Computational Fluid Dynamics

Philipp Bekemeyer*, Reik Thormann†, Sebastian Timme‡

University of Liverpool, School of Engineering, England, United Kingdom

The numerical investigation of dynamic responses to atmospheric turbulence is an important task during the aircraft design and certification process. Efficient methods are desirable since large parameter spaces spanned by e.g. Mach number, flight altitude, load case and gust shape need to be covered. Aerodynamic non-linearities such as shocks and boundary layer separation should be included to account for transonic flight conditions. A linearised frequency-domain method is outlined to efficiently obtain gust responses using computational fluid dynamics. The Reynolds-averaged Navier–Stokes equations are linearised around a steady-state solution and solved for discrete frequencies. The resulting large but sparse system of linear equations can then be evaluated significantly faster than its time-domain counterpart. The method is verified analysing sinusoidal gust responses for an aerofoil and a large civil aircraft considering a broad range of reduced frequencies. Derivatives of aerodynamic coefficients and complex-valued surface pressures are compared for time- and frequency-domain approaches. Next, 1-cos gusts are investigated using an incomplete inverse Fourier transform in conjunction with a complex-valued weighting function to discuss time histories of lift coefficients as well as surface pressures. Finally, introduced techniques are applied to conditions arising from certification requirements to demonstrate the technical readiness. The methods discussed present an important step to establish computational fluid dynamics in the routine aircraft loads process.

Nomenclature

C_L	=	lift coefficient
C_M	=	pitching-moment coefficient
c_p	=	pressure coefficient
c_f	=	skin-friction coefficient
c	=	chord length
I	=	identity matrix
L_g	=	gust length
$\mathbf{R}$	=	vector of non-linear residual functions
U_∞	=	freestream velocity
$\mathbf{v}_g$	=	**vector of gust disturbances**
$\mathbf{w}$	=	vector of conservative variables
$\mathbf{x}$	=	vector of grid point locations
$\dot{\mathbf{x}}$	=	vector of grid point velocities
x_0	=	gust off-set
ε	=	finite difference step-size
ω^*	=	**reduced frequency**
$\boldsymbol{\varphi}$	=	**vector of phase shifts**
Ξ	=	complex-valued weighting function

I. Introduction

During aircraft design and certification **many thousands** of dynamic responses due to atmospheric turbulence need to be investigated, and thus efficient and reliable tools are required. Since the vast majority of commercial aircraft operate at transonic cruise speeds, these tools should be able to account for aerodynamic non-linearities, such as recompression shocks and boundary layer separation, to predict airframe loads accurately. Linear poten-

*Ph.D. Student, AIAA Student Member, philipp.bekemeyer@liverpool.ac.uk
†Research Associate, reik.thormann@liverpool.ac.uk
‡Lecturer, AIAA Member, sebastian.timme@liverpool.ac.uk

tial flow equations, mostly the doublet lattice method [1], are current industrial practice and predict unsteady aerodynamic loads uncoupled from the steady flow field. Dynamic responses due to gust excitation are analysed using a frequency-domain sampling process and afterwards projecting the obtained surface forces onto the structural modes. While offering fast and robust dynamic response predictions, aforementioned aerodynamic non-linearities are neglected. Thus, especially at transonic flow conditions, linear potential methods are not predicting loads conservatively, which either requires correction techniques or more accurate simulation tools to be applied.

Computational fluid dynamics (CFD) is offering more accurate results at non-linear conditions and, with increasing computational resources, has become a feasible alternative. Gust response simulations of large aircraft configurations have been accomplished solving the governing equations in an unsteady time-marching approach [2]. However, due to overwhelming computational cost even for a single simulation, this approach quickly becomes prohibitive in an industrial environment. **Instead, within the range of their validity linearised frequency-domain, also known as time-linearised, methods offer a large efficiency improvement while maintaining the accuracy of the underlying non-linear CFD model.**

Time-linearised methods were initially applied in the field of turbomachinery to model oscillatory blade motion inside a cascade [3, 4, 5]. The Euler equations are linearised around a non-linear steady-state solution assuming small amplitude harmonic motion. The first harmonic of the perturbation is compared with unsteady time-marching approaches [6, 7], showing excellent agreement at several orders of magnitude reduced computational cost. Results for external flows are presented for an aerofoil undergoing forced-motion excitation [8]. Forced-motion responses are also published for an aerofoil, a wing and an aircraft in [9], while a delta wing is discussed in [10] analysing small harmonic oscillations of elastic modes and control surfaces. A significant speed-up compared with the unsteady non-linear Euler equations solved in a time-marching approach is reported throughout.

Initial work solving the Reynolds-averaged Navier-Stokes (RANS) equations has again

been published in the field of turbomachinery [11], showing good agreement between numerical simulations and experimental data for stall flutter including large separation in a blade cascade. Analysing forced-motion responses for external flows, time-saving factors between one and two orders magnitude have been reported for aerofoils and wings [12, 13, 14]. A similar decrease in cost was also demonstrated for a full civil aircraft at cruise conditions [15]. **Independently of each other, several authors recently proposed an extension of the frequency-domain method towards gust response simulations [16, 17, 18]. In [17] frequency-domain results are projected onto structural modes and a rational function approximation is applied to analyse aperiodic 1-cos gust responses. Instead, the current work proposes a direct complex-valued superposition of frequency-domain response data which allows the analysis of aerodynamic gust responses independently of structural dynamics.**

After outlining the theory, the time-linearised gust approach is verified for several test cases. Results are first presented for an aerofoil in sub- and transonic attached-flow conditions and further in a challenging post-buffet, detached-flow situation. The validity of the method at a broad range of reduced frequencies is ensured by comparing transfer functions of lift coefficient. Furthermore, complex-valued surface pressure distributions and influence of the gust amplitude are analysed to discuss the assumption of a dynamically linear response. Secondly, results are shown for a large civil aircraft at cruise conditions, again comparing complex-valued surface pressures and global coefficients. Thirdly, 1-cos gust excitations, as defined by international certification requirements, are discussed to demonstrate the maturity of the method for industry-relevant applications.

II. Method Formulation

A. Time-Linearised Aerodynamics

This section outlines the theory behind the time-linearised gust approach and the complex-valued superposition to obtain aperiodic time-domain responses. All presented equations contain only terms relevant to gust response to keep the theory section as concise as possible. The governing equations in semi-discrete vector form, representing the non-linear RANS equations as arising from the CFD formulation, are written as

$$\dot{\mathbf{w}} = \mathbf{R}(\mathbf{w}, \mathbf{v}_\mathrm{g}) \tag{1}$$

where $\mathbf{w}$ denotes **the vector of conservative variables**, $\mathbf{R}$ is the non-linear residual corresponding to the unknowns and $\mathbf{v}_\mathrm{g}$ indicates external disturbances due to various gusts.

The difference between the vector of conservative variables $\mathbf{w}$ and an equilibrium solution $\mathbf{w}_0$ is introduced as

$$\Delta\mathbf{w} = \mathbf{w} - \mathbf{w}_0 \tag{2}$$

and accordingly for external disturbances $\Delta\mathbf{v}_\mathrm{g} = \mathbf{v}_\mathrm{g} - \mathbf{v}_{\mathrm{g}0}$. Assuming small perturbations, a first-order Taylor expansion is applied around the equilibrium point

$$\frac{\mathrm{d}\Delta\mathbf{w}}{\mathrm{d}t} = \mathbf{R}(\mathbf{w}_0, \mathbf{v}_{\mathrm{g}0}) + \frac{\partial\mathbf{R}}{\partial\mathbf{w}}\Delta\mathbf{w} + \frac{\partial\mathbf{R}}{\partial\mathbf{v}_\mathrm{g}}\Delta\mathbf{v}_\mathrm{g} \tag{3}$$

where $\frac{\partial\mathbf{R}}{\partial\mathbf{w}}$ describes the Jacobian matrix with respect to all fluid unknowns and $\frac{\partial\mathbf{R}}{\partial\mathbf{v}_\mathrm{g}}$ denotes changes in residual due to gust excitation. **Since all derivatives are formed around the same equilibrium point,** $|_{\mathbf{w}_0,\mathbf{v}_{g0}}$ **is omitted in the notation. The first term on the right-hand side of the latter equation is equivalent to the non-linear steady flow residual which accounts for aerodynamic non-linearities and is assumed to be converged to machine precision. While the steady flow solutions converge sufficiently for all presented cases in this paper, a linearised system can be solved also for steady flow fields not fully converged. However, the achieved accuracy highly**

depends on the investigated flow conditions. A rough and initial investigation is presented in [19] reporting still fair agreement close to the buffet onset.

Subsequently, the system is transferred into frequency domain assuming the disturbance vector $\Delta\mathbf{w}$ and external excitation vector $\Delta\mathbf{v}_\mathrm{g}$ change harmonically in time. Thus, Eq. (3) becomes after re-arranging

$$\left(\frac{\partial\mathbf{R}}{\partial\mathbf{w}} - i\omega^* I\right)\hat{\mathbf{w}} = -\frac{\partial\mathbf{R}}{\partial\mathbf{v}_\mathrm{g}}\hat{\mathbf{v}}_\mathrm{g} \tag{4}$$

with $\hat{\mathbf{w}}$ and $\hat{\mathbf{v}}_\mathrm{g}$ denoting complex-valued Fourier coefficients. **The reduced frequency ω^* is normalised using the reference chord length c_ref and the freestream velocity U_∞.**

Applying the chain rule, the right-hand side in Eq. (4) becomes

$$\frac{\partial\mathbf{R}}{\partial\mathbf{v}_\mathrm{g}}\hat{\mathbf{v}}_\mathrm{g} = \frac{\partial\mathbf{R}}{\partial\dot{\mathbf{x}}}\frac{\partial\dot{\mathbf{x}}}{\partial\mathbf{v}_\mathrm{g}}\hat{\mathbf{v}}_\mathrm{g} \tag{5}$$

where $\dot{\mathbf{x}}$ describes the artificial mesh velocities applied to model the gust during the CFD calculation using the field velocity method [20]. Since the relation between gust disturbance $\mathbf{v}_\mathrm{g}$ and artificial mesh velocity $\dot{\mathbf{x}}$ is simply

$$\dot{\mathbf{x}} = -\mathbf{v}_\mathrm{g} \tag{6}$$

the right-hand side term can be written as

$$\frac{\partial\mathbf{R}}{\partial\mathbf{v}_\mathrm{g}}\hat{\mathbf{v}}_\mathrm{g} = -\frac{\partial\mathbf{R}}{\partial\dot{\mathbf{x}}}\hat{\mathbf{v}}_\mathrm{g} \tag{7}$$

A finite-difference evaluation

$$\frac{\partial\mathbf{R}}{\partial\dot{\mathbf{x}}}\hat{\mathbf{v}}_\mathrm{g} = \frac{\mathbf{R}(+\varepsilon\hat{\mathbf{v}}_\mathrm{g}) - \mathbf{R}(-\varepsilon\hat{\mathbf{v}}_\mathrm{g})}{2\varepsilon} \tag{8}$$

with a known gust shape vector $\hat{\mathbf{v}}_\mathrm{g}$ and ε as the finite-difference step size is used to solve Eq. (7) without computing the matrix explicitly. The cost of two additional

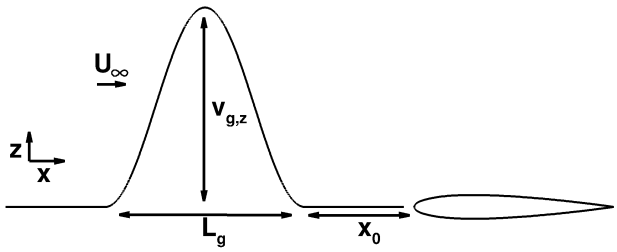

Figure 1. Sketch of gust parameters

residual evaluations is necessary to construct the right-hand side before solving the linear system, while the computational overhead of forming and storing the matrix explicitly can be avoided.

Furthermore, an analytical description of the gust vector is introduced as

$$\hat{\mathbf{v}}_{\mathrm{g}}(\mathbf{x}, \omega^*) = v_{gz} e^{i\boldsymbol{\varphi}(\mathbf{x},\omega^*)} \tag{9}$$

where v_{gz} and $\boldsymbol{\varphi}(\mathbf{x}, \omega^*)$ denote the constant vertical gust amplitude and the phase shift vector according to the spatial location vector x, respectively. The phase shift can either be obtained from a Fourier transform of a sinusoidal time-domain signal or, more easily and based on linear potential theory [21], using the expression

$$\boldsymbol{\varphi}(\mathbf{x}, \omega^*) = (\mathbf{x} + x_0) \frac{\omega^*}{c_{\mathbf{ref}}} \tag{10}$$

where x_0 is the initial distance between gust and airframe. All gust parameters are visualised in Fig. 1. The initial distance x_0 can be chosen arbitrarily while it is common to let the gust start close to the airframe to save computational time, but not too close to avoid errors during the first few time-steps. Similar expressions can also be derived for lateral gusts by applying the corresponding amplitude and modifying the phase shift accordingly.

Once the discrete frequency response function is calculated, results to arbitrary gust excitations Δw can be obtained applying a superposition in conjunc-

tion with a complex-valued weighting function denoted by $\Xi(\omega^*)$

$$\Delta \mathbf{w} = \sum_j \Re\left(\Xi(\omega_j^*)\hat{\mathbf{w}}_j e^{i\omega_j^* t}\right) \tag{11}$$

where $\Re$ describes the real part of the following complex-valued coefficients. While the linearised solutions $\hat{\mathbf{w}}_j$ are independent of the aperiodic gust shape of interest, only the weighting function needs to be re-computed using a Fourier transform on the excitation signal.

In general, non-periodic time-domain signals include an infinite range of frequencies. However, assuming the magnitude of the excitation as a function of reduced frequency is decaying, an incomplete, inverse Fourier transformation can be applied considering only dominant frequencies. The time- and frequency-domain representations for three different excitation types are shown in Fig. 2. For sinusoidal gusts, only the frequency corresponding to the wavelength is of interest. Contrary, both other signals excite an infinite range of frequencies. While the 1-cos gust exhibits roots at several frequencies, the pulse excitation shows no roots in the analysed frequency range [22]. The mathematical description of the pulse excitation as well as its application to obtain dynamic derivatives efficiently using CFD is presented in [23]. If the frequency response function is created from a time-marching approach, the pulse function is computationally more efficient compared to single-frequency excitation analysis since only one simulation is required.

B. Computational Fluid Dynamics Method

Simulations for all presented test cases are performed using the DLR-TAU code [24] solving the RANS equations in conjunction with the Spalart–Allmaras turbulence model [25]. Inviscid fluxes are discretised applying a central scheme with the scalar artificial dissipation of Jameson, Schmidt and Turkel [26]. Exact gradients used for viscous and source terms are computed using the Green–

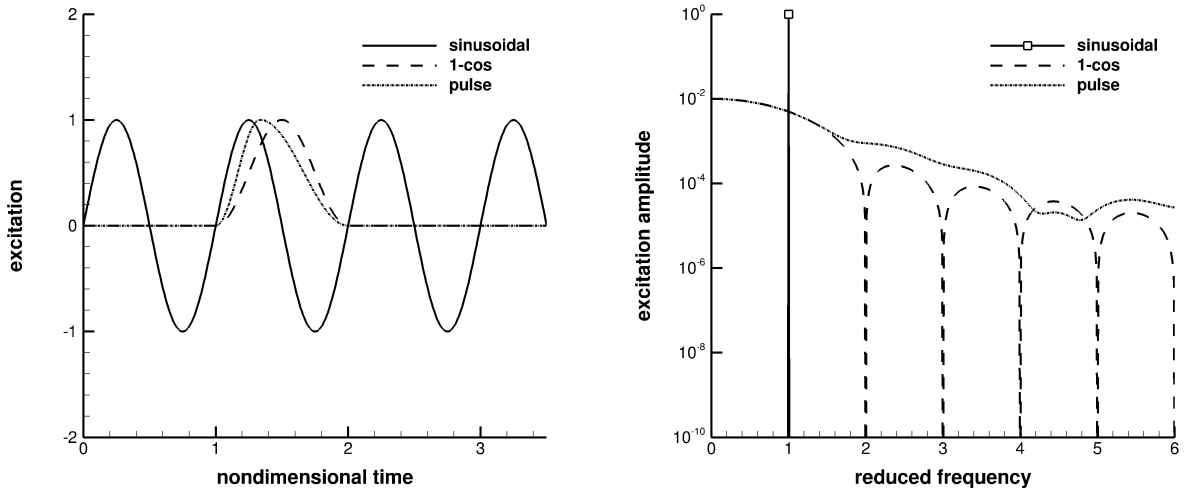

a) Time domain b) Frequency domain

Figure 2. Excitation signals represented in time and frequency domain

Gauss approach. Steady-state solutions are obtained utilising the backward Euler method with lower-upper Symmetric–Gauss–Seidel iterations [27] and local time-stepping. Convergence is accelerated further by applying a case-dependent multigrid scheme. During unsteady simulations a dual time-stepping combined with the second order backward differentiation formula is used. Gusts are included using the field velocity approach which introduces an artificial mesh velocity [20]. The velocity term is added to the governing equations and is prescribed based on the gust excitation while no deformation of the computational grid is required.

Time-domain solver settings are summarised in Tab. 1. For the investigation of sinusoidal excitations, the unsteady time-step size is chosen indirectly by defining the number of steps per period. Analysing 1-cos gust excitations, time-step size and number of time steps follow from numerical experiments. For pulse excitations the number of steps is increased by a factor of four while the time-step size is halved compared with a 1-cos excitation. Further when a Cauchy convergence criterion is applied, a tolerance of 10^{-8} for the relative error of the drag coefficient, in addition to an abort criterion based on the density residual

	excitation	cases 1/2	case 3	aircraft case
Abort density residual	both	10^{-3}	10^{-5}	10^{-3}
Cauchy convergence crit.	both	✓	×	✓
Multigrid cycle scheme	both	3w++	sg	2v
Time-steps per period	sine	64	128	128
Number of periods	sine	10	15	15
Time-step size	1-cos	0.02	0.02	0.0015 s
Number of time-steps	1-cos	3000	3000	1280

Table 1. Time-domain numerical parameters

	cases 1/2	case 3	aircraft case
Number of Krylov vectors	30	40	100
Number of deflation vectors	10	15	20
Abort density residual	10^{-8}	10^{-8}	10^{-6}

Table 2. Frequency-domain numerical parameters

is used.

The linearised frequency-domain formulation is based on a first-discretise-then-linearise, matrix-forming approach with an analytical, hand-differentiated Jacobian matrix. Linear systems arising from this approach are solved using a generalised conjugate residual solver with deflated restarting [28]. In all cases a block incomplete lower-upper factorisation of the Jacobian matrix with zero level of fill-in is applied for preconditioning [29]. The number of Krylov vectors used to solve each linear system together with the linear convergence criteria are given in Tab. 2. The higher number of vectors for aerofoil case 3 compared to cases 1 and 2 accounts for the increased stiffness of the linear system caused by the large shocked-induced separation.

The DLR-TAU code is widely used in the European aerospace sector and validations of the code are available in the literature for steady [24, 30] as well as unsteady cases [30, 31]. Since the time-linearised method provides results identical to the unsteady time-marching RANS equations for small amplitudes, results in this paper are compared with their time-domain counterparts rather than experimental data. Further, experimental data for harmonic gust excitations are

test case	Mach number	angle of attack (deg)	attached flow
case 1	0.3	0.0	✓
case 2	0.8	0.0	✓
case 3	0.8	3.0	✗

Table 3. Description of test cases for NACA0012 aerofoil

currently not available in the literature to the authors knowledge.

III. Aerofoil Results

Results are presented for a NACA0012 aerofoil using a **mesh consisting of 70,000** grid points with a first wall-normal spacing of one or less in wall units. Two attached-flow cases (case 1 and 2) and one post-buffet, detached-flow case (case 3) are investigated with a Reynolds number of ten million. Mach number and angle of attack for all cases are given in Tab. 3. The steady-state surface pressure distribution is shown in Fig. 3a for all three cases **after converging the density residual to machine precision**. While no shock is present for case 1, both transonic-flow cases feature a strong shock. In case 3 the strong shock causes the flow to detach, resulting in a negative skin friction coefficient from the shock foot to the trailing edge as presented in Fig. 3b.

The linearised frequency-domain (LFD) method is **verified** at several reduced frequencies by comparing frequency response functions of the lift coefficient to equivalent time-domain (TD) results. Instead of producing TD solutions separately for each frequency of interest, a pulse signal is used to excite all relevant frequencies during one unsteady time-marching simulation. A Fourier transform of the unsteady lift coefficient is then performed and resulting complex-valued Fourier coefficients are weighted by the Fourier transform of the pulse excitation signal. A dynamically linear response is ensured by setting the gust excitation velocity to 0.001% of the freestream velocity. Perfect agreement between both simulation methods is observed throughout for real and imaginary parts as seen in Fig. 4. Real and imaginary parts for both attached-flow cases show only positive values in the investigated frequency range, whereas a change of sign in the real part and a maximum in the

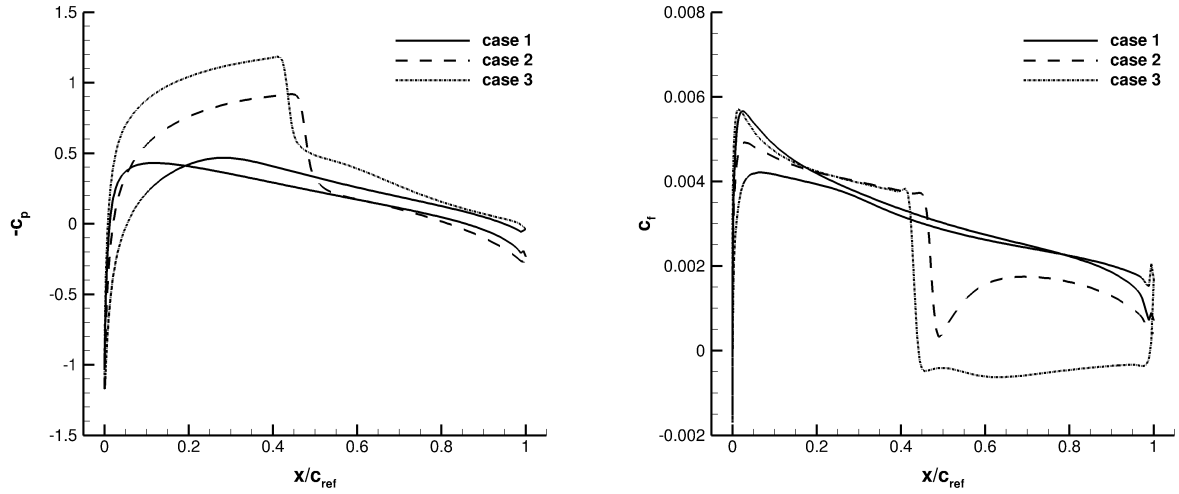

a) Surface pressure distribution b) Skin-friction distribution

Figure 3. Steady-state surface pressure and skin-friction distribution for NACA0012 aerofoil

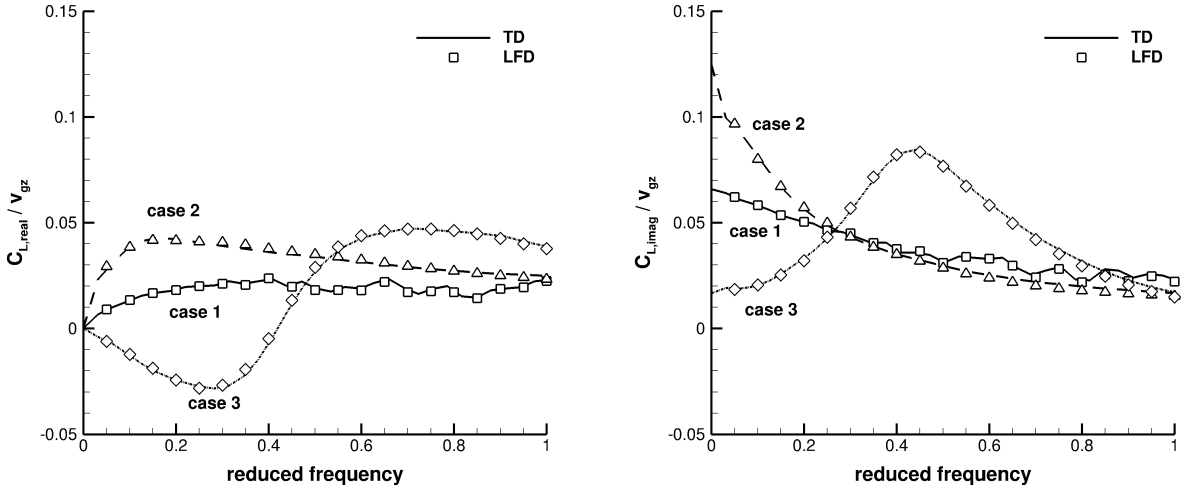

a) Real part b) Imaginary part

Figure 4. Frequency response functions of lift coefficient for aerofoil test cases

imaginary part is present for case 3 at a reduced frequency of about 0.5. Similar behaviour has been presented for forced-motion simulations close to the buffet onset [32, 33, 34].

Complex-valued surface pressure distributions for all three aerofoil cases obtained from LFD simulations are compared with their corresponding TD counterparts in Fig. 5. **A reduced frequency of 0.2, randomly chosen, is investigated for all flow conditions.**

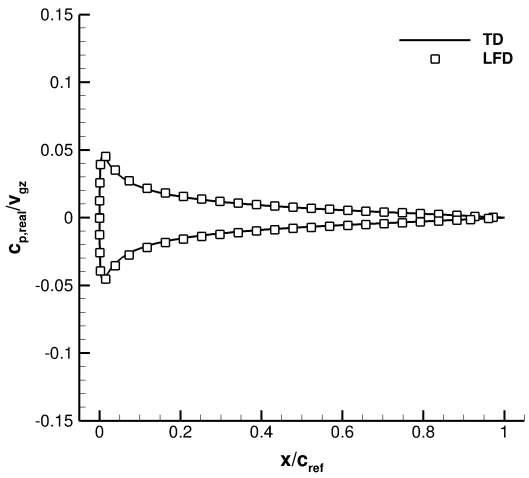

a) Real part case 1

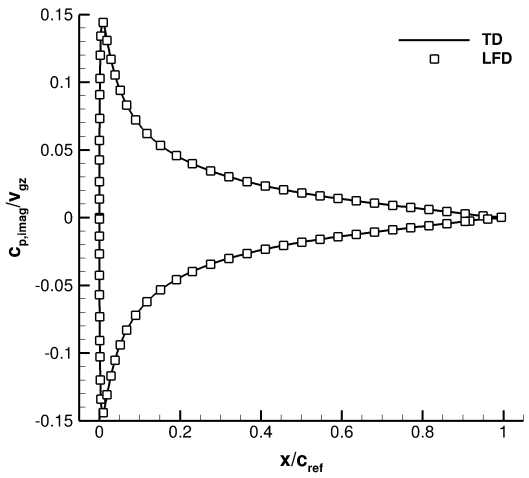

b) Imaginary part case 1

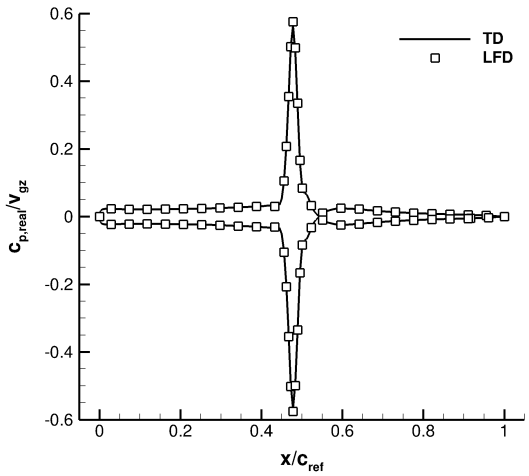

c) Real part case 2

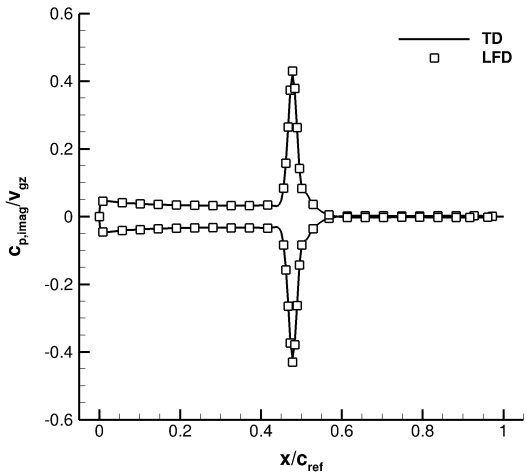

d) Imaginary part case 2

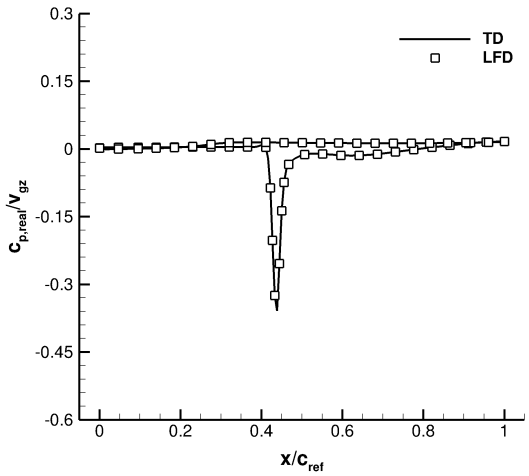

e) Real part case 3

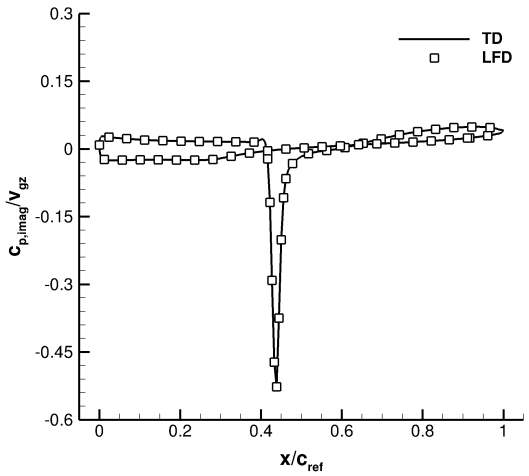

f) Imaginary part case 3

Figure 5. Complex-valued surface pressure coefficients for sinusoidal gust with ω^*=0.2.

Results from TD are produced applying a Fourier transform to the instantaneous surface pressures, omitting the initial transient response. All values are normalised by the gust excitation amplitude. Maximum values in the subsonic case are located around the leading edge in real as well as imaginary parts and excellent agreement between both simulations is observed in Figs. 5a and 5b. For case 2 the highest amplified region is around the shock location, as shown in Figs. 5c and 5d for real and imaginary parts, respectively. Again, coinciding results between the TD and LFD approach are obtained. Even at the severe flow conditions of case 3, including a strong shock followed by a large area of shock-induced boundary layer separation, excellent agreement is achieved as visualised in Figs. 5e and 5f. Even though not shown here, results at different reduced frequencies are as satisfying as the ones presented.

In terms of computational cost the frequency-domain solve is between one to two orders of magnitude faster than the corresponding non-linear time-marching solution for both attached-flow cases. While unsteady time-marching simulations are highly affected by the investigated flow topology, resulting in increased computational cost at severe flow conditions, the frequency-domain approach is much less sensitive provided a robust linear solver is applied. Indeed, even higher time-saving factors are achieved for case 3.

The amplitude of the lift coefficient, normalised using the linearised response and considering the first harmonic only for TD data, over gust amplitude is shown in Fig. 6. Naturally, a constant line is obtained from the LFD approach whereas non-linear time-marching solutions start to differ with increasing gust amplitude. These differences are a measure of non-linearity induced by the increased amplitude. For all cases, results coincide for very small gust amplitudes, demonstrating that the linearised method is capable of fully reproducing dynamically linear responses. With increasing amplitude of gust excitation, the resulting magnitude of the lift coefficient decreases in cases 1 and 3, while for the transonic attached-flow case no significant drop is observed. Once amplitudes are high enough to cause either significant shock movement or separation, the unsteady lift increases extensively in

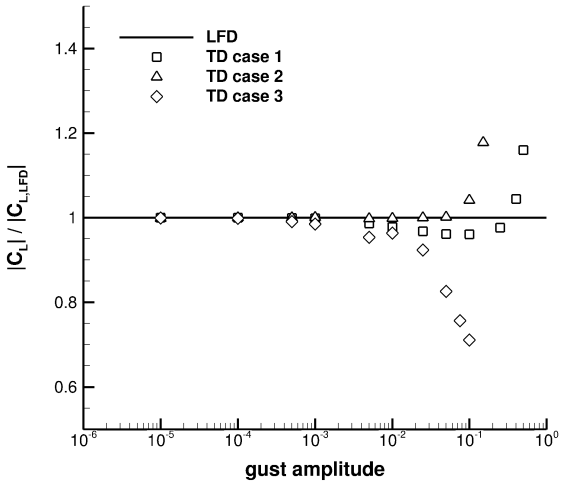

Figure 6. Amplitude of lift coefficient over gust amplitude for sinusoidal gust with ω^*=0.2

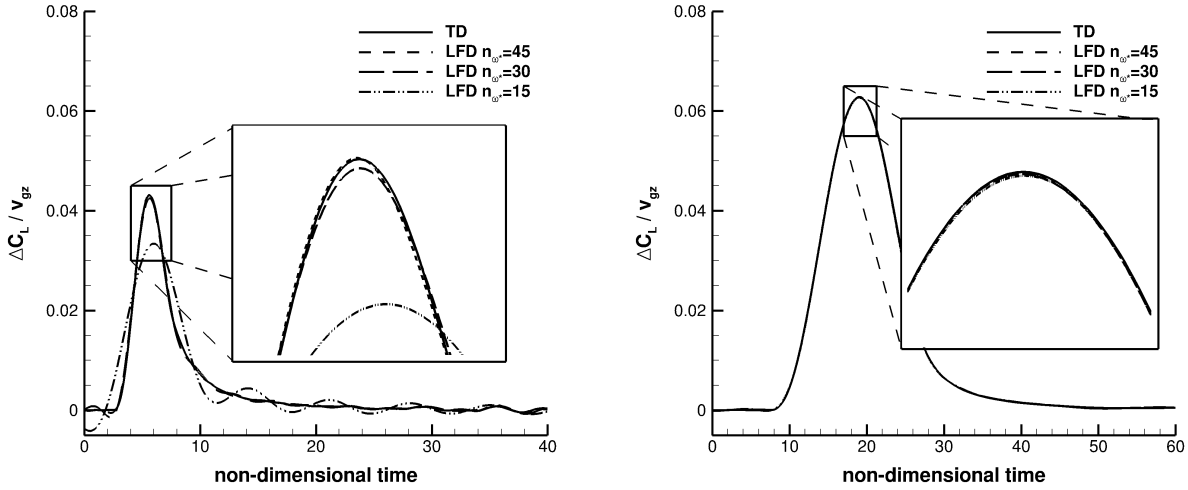

a) $\mathbf{L_g/c_{ref} = 5}$ **b)** $\mathbf{L_g/c_{ref} = 20}$

Figure 7. Change in lift coefficient scaled by gust amplitude due to 1-cos gusts for case 1 with varying number of retained frequencies

case 1 and 2. In case 3 on the other hand, the separation area increases with increasing gust amplitudes and thus generated lift decreases.

Responses to 1-cos gusts excitation are finally obtained by an incomplete inverse Fourier transform of several discrete frequency-domain results in conjunction with a complex-valued weighting function as outlined in Sec. II. **The influence of the reduced frequencies, retained during the inverse Fourier transform, is analysed for two different gust**

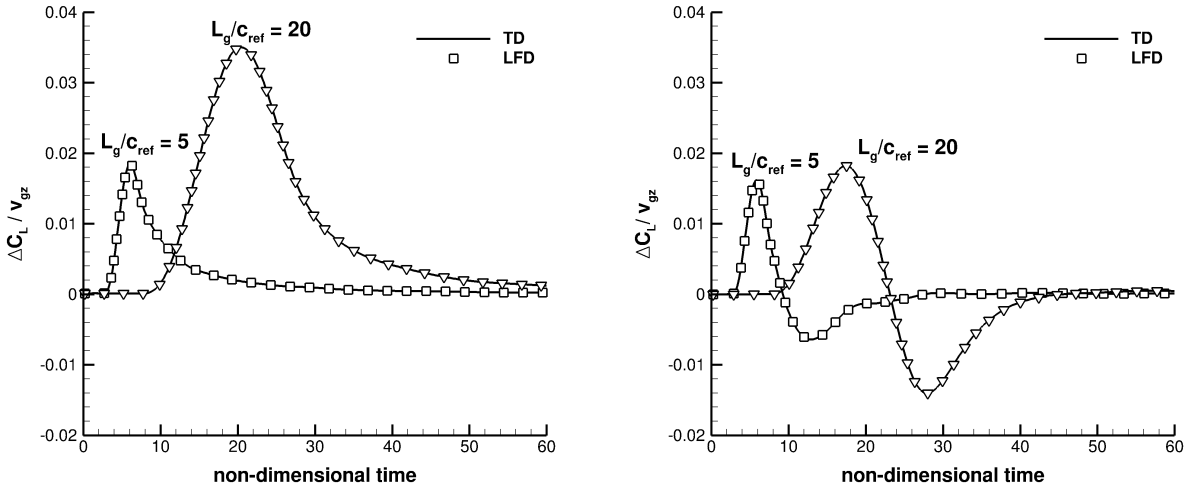

a) case 2 b) case 3

Figure 8. Change in lift coefficient scaled by gust amplitude for 1-cos gusts with different gust lengths

lengths for case 1 in Fig. 7 with a constant gust amplitude of 1% of the freestream velocity. With the spacing kept constant at $\Delta\omega^* = 0.01$ and sampling always starting at $\omega^* = 0$, the number of frequencies n_{ω^*} is varied between 15, 30 and 45. For shorter gust lengths a higher number of frequency-domain results is necessary to accurately predict loads, while with increasing gust length the affected frequency range is reduced. Thus, 45 equally spaced reduced frequencies are needed for $L_g/c_{\mathbf{ref}} = 5$ to achieve an error $\frac{\Delta C_{L,LFD,max} - \Delta C_{L,TD,max}}{\Delta C_{L,TD,max}}$ below 1%, while this number decreases to 15 for $L_g/c_{\mathbf{ref}} = 20$. Although not shown here, the influence of the step size $\Delta\omega^*$ is analysed as well. Whereas for shorter gust length a larger step size is preferable, the applied step size can be reduced significantly if only long gusts are of interest. However, the sampling process including the choices of $\Delta\omega^*$ and n_{ω^*} highly depends on the aperiodic gust of interest analysed afterwards.

Dynamic results for both other cases are shown in Fig. 8 in comparison to the corresponding unsteady time-marching results for non-dimensional gust lengths of $L_g/c_{\mathbf{ref}} = 5$, 10 and 20. While the gust amplitude for the transonic, attached-flow case is 1% of the freestream velocity, for the detached-flow case a reduced

value of 0.001% of the freestream velocity is used to ensuring a dynamically linear response. Overall good agreement between both solution methods for all gust lengths is observed. Computational cost, if 45 samples are computed, is equivalent to one unsteady time-marching simulation. However, based on this sampling data, various gust parameters of interest, e.g. gust shape, gust length and gust off-set, can be analysed at minimal extra cost provided the affected frequency range is covered. On the contrary, the time-domain analysis needs to be redone for each gust-parameter change.

IV. Large Civil Aircraft Results

The final presented test case is a large civil aircraft. The computational mesh consists of 130,000 points on the surface and nearly 8 million points throughout the computational domain. A steady-state solution **at a Mach number of** 0.8 **and an altitude of** 10 **km** is obtained using an elastic trimming procedure based on Broyden's method [35], which balances lift and weight while ensuring zero pitching moment. The **steady** simulation includes 94 structural modes to represent elastic deformation while for trimming an artificial mode for the elevator deflection is used. The elevator deflection and angle of attack are iteratively adjusted until the desired coefficients are reached **while applying the radial basis function method to deform the computational grid** [36]. **After each iteration step surface loads are projected onto the structural degrees of freedom to determine the structural deformation and subsequently deform the mesh. The final surface mesh, after driving the density residual to converge seven orders of magnitude, is visualised in Fig.** 9a. A strong shock along the wingspan at roughly 70% chord length can be seen in the steady surface pressure distribution in Fig. 9b. Furthermore, the effects of the first wing bending mode in conjunction with the torsion mode cause a decrease of sectional lift towards the wing tip. The elevator is deflected during the trimming process resulting in a strong suction area around the leading edge but no shock formation.

First, the convergence behaviour of the density residual as well as the complex-valued

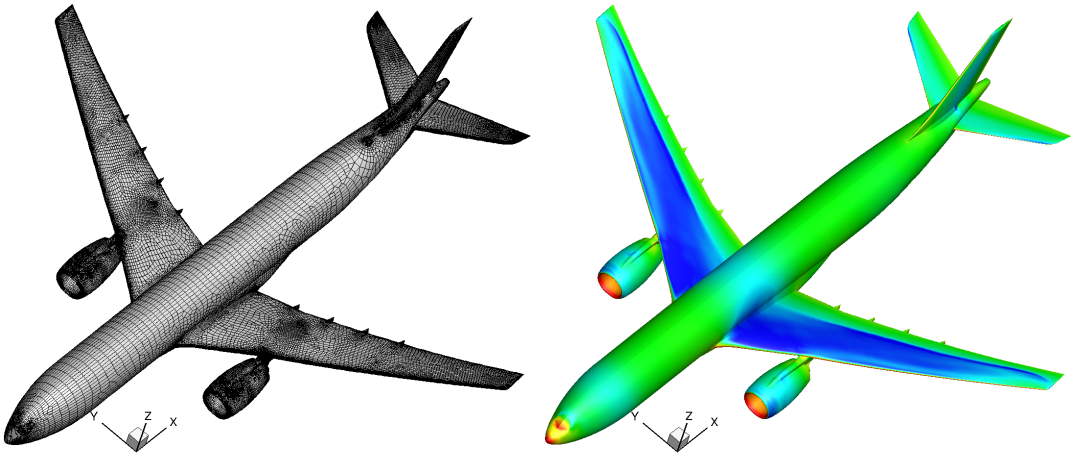

a) Surface point distribution **b) Steady surface pressure distribution**

Figure 9. Surface mesh and steady-state surface pressure coefficient for civil aircraft

coefficients of lift and pitching moment are analysed while solving the frequency-domain system for **a reduced frequency of** 0.073. Results are presented in Fig. 10 with coefficients normalised by their converged values. Once the residual has converged five orders of magnitude, both coefficients remain essentially unchanged. Therefore, if only integrated loads are of interest, simulations can be stopped earlier, resulting in an additional time-saving of 50% compared with fully converging the system. For the remainder of the discussion, the density residual is driven to drop six orders of magnitude, ensuring converged solutions for integrated loads as well as surface pressures.

Investigating the same reduced frequency as before, the influence of the finite-difference step size ε when forming the right-hand side in Eq. (8) is analysed. Figure 11 shows the magnitudes of lift and pitching moment coefficients, normalised to converge towards one, for a range of finite-difference step sizes. Results independent of the step size are obtained below 10^{-3} for both coefficients, while larger values result in increasing magnitudes with a higher impact on the moment. A value of 10^{-4} is applied throughout in the following discussion to ensure step-size independent results.

Comparing frequency response functions of lift and pitching moment coefficients, the quality of the presented method is shown at several reduced frequencies for the complex three-dimensional test case. Similar to the aerofoil test cases, a gust pulse excitation is used

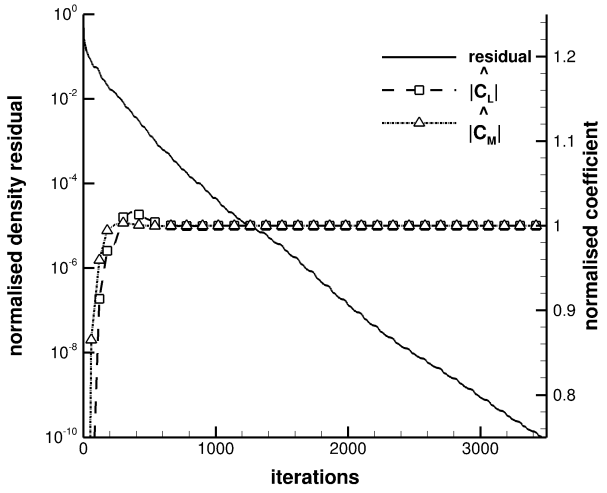

Figure 10. Linear convergence of frequency-domain gust approach

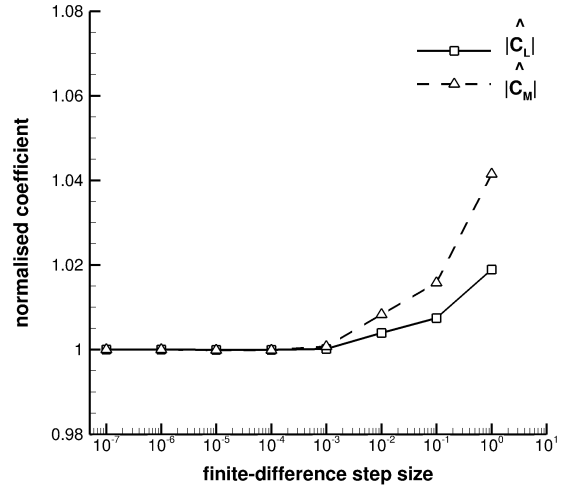

Figure 11. Influence of finite-difference step size

to obtain the frequency response function with just one unsteady time-marching simulation. A Fourier transform of the unsteady coefficients of lift and pitching moment is performed and resulting complex-valued Fourier coefficients are weighted by the Fourier transform of the input signal. The amplitude of the excitation during the time-marching simulation is set to 0.001% of the freestream velocity, ensuring a linear dynamic response. Real and imaginary parts of the coefficients, presented in Figs. 12a and 12b, show excellent agreement at all frequencies between time- and frequency-domain predictions.

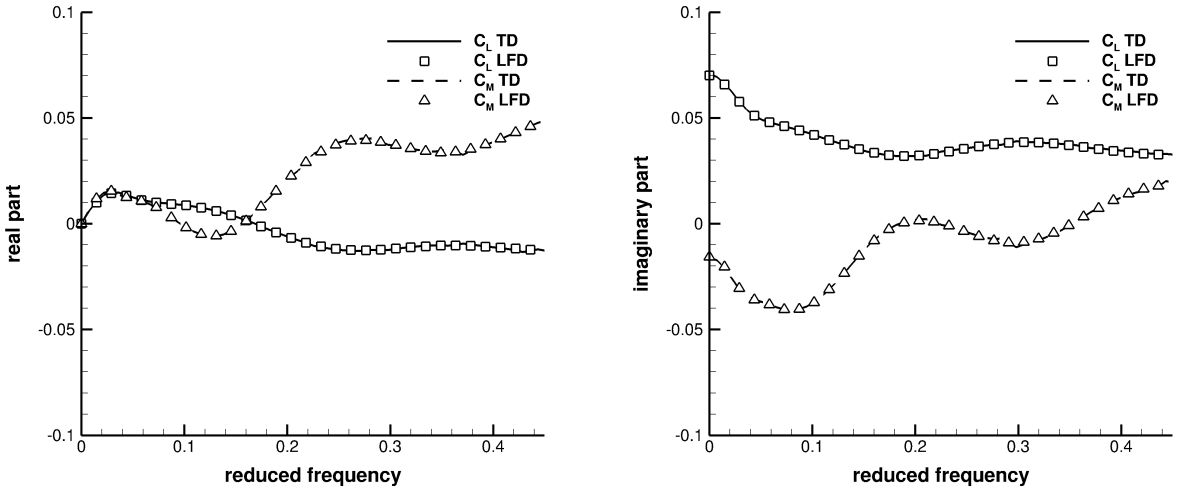

a) Real part **b) Imaginary part**

Figure 12. Frequency response functions of lift and moment coefficients

Complex-valued surface pressure distributions are compared at a reduced frequency of 0.073 to analyse the LFD gust method in more detail. Reference time-domain solutions are generated simulating a sinusoidal gust with an excitation amplitude of 0.001% of the freestream velocity for 15 periods and then performing a Fourier transform on the instantaneous surface pressures during the final period. Frequency-domain solutions on the other hand are readily available once the linear system is solved. Starboard-wing results are displayed in Figs. 13a and 13b for real and imaginary parts with solid and dashed lines denoting time- and frequency-domain solutions, respectively. Even at challenging flow topologies good agreement between both methods is obtained. Around the shock at 70% chord length on the upper surface the highest pressure perturbations occur, again with no differences between the simulations. Excellent agreement is observed also around the wing-pylon junction, which causes complex flow behaviour due to vortices. In addition, results are compared for the elevator and fin in Figs. 13c and 13d with similar good agreement. Highest perturbations are located around the leading edge caused by the suction area since no shock formation is present.

Results are also compared by extracting slices from the wing and elevator surfaces, the locations of which are indicated by black lines in Fig. 13. Real and imaginary parts are nor-

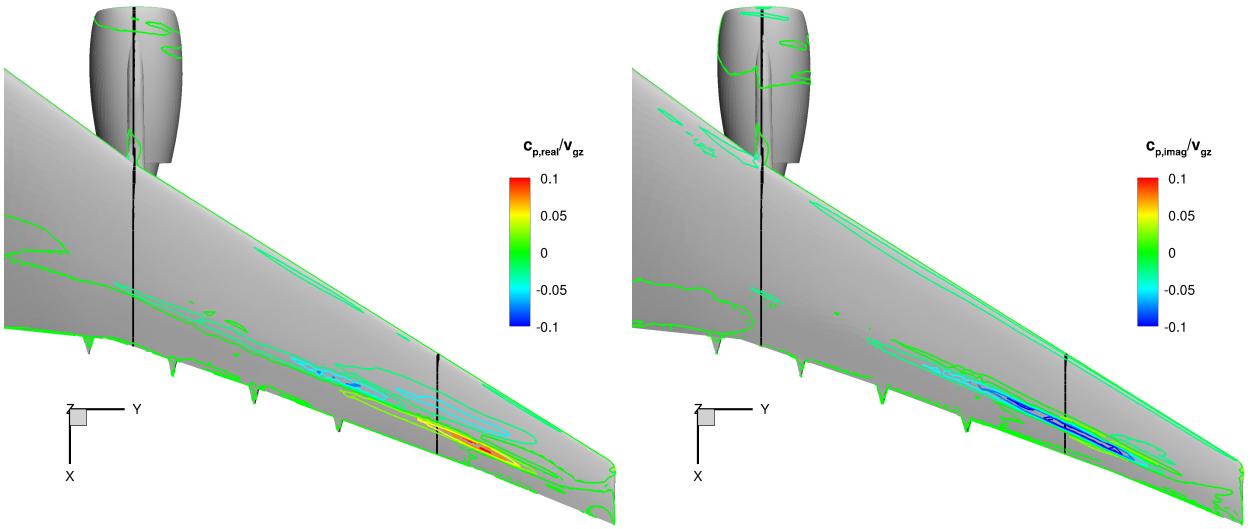

a) Real part on starboard wing **b) Imaginary part on starboard wing**

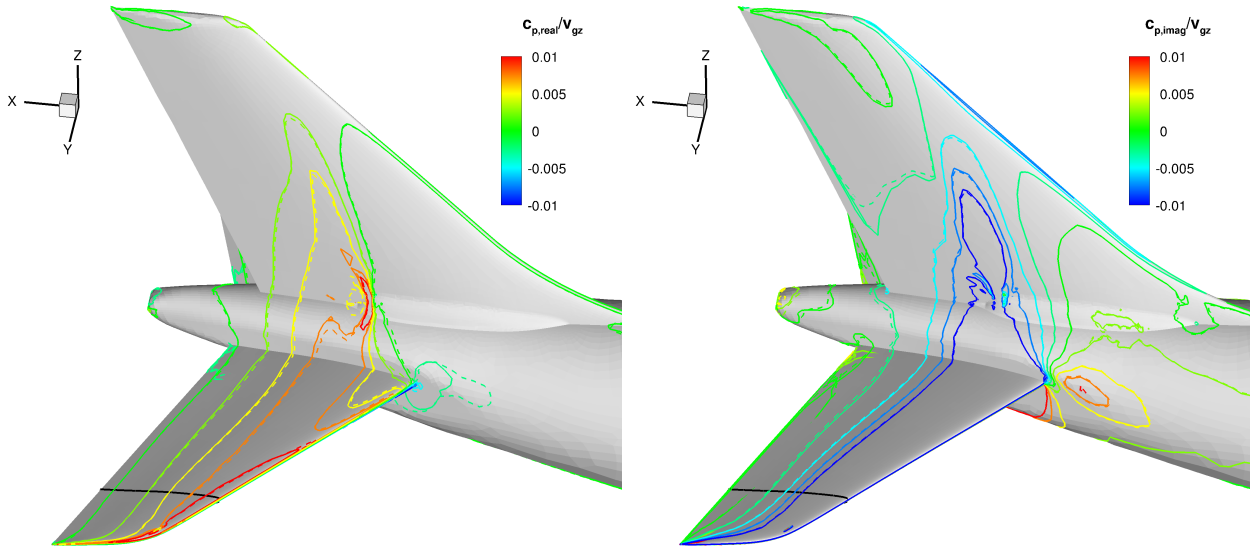

c) Real part on tail **d) Imaginary part on tail**

Figure 13. Complex-valued surface pressures for sinusoidal gust with $\omega^* = 0.073$ showing time- and frequency-domain results as solid and dashed lines, respectively. Black lines indicate locations of extracted sections.

malised by the excitation amplitude, while the x-axis is scaled by the local chord length. Figures 14a and 14b present complex-valued pressures for the first slice at 75% semi-wingspan, showing good agreement between the two simulation techniques. The overall trend is similar to the previously discussed aerofoil results of case 3 with maximum values around the shock location. Some minor differences occur between LFD and TD simulations at the shock location for both real and imaginary components. Reducing the excitation amplitude further

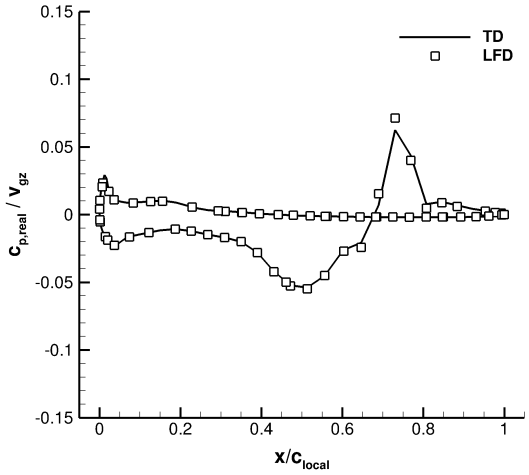

a) Real part at 75% semi-wingspan

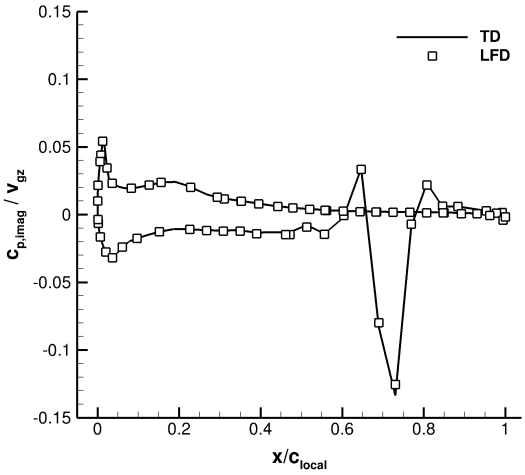

b) Imaginary part at 75% semi-wingspan

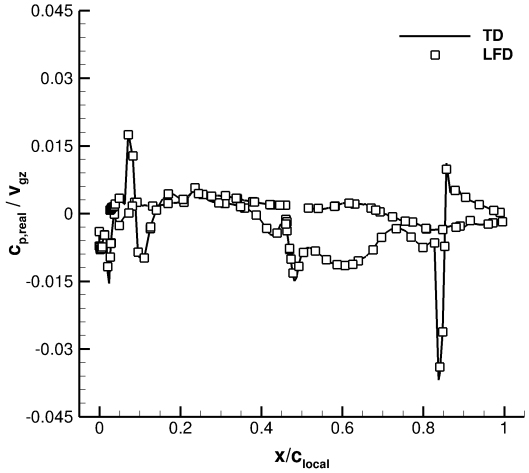

c) Real part at 32% semi-wingspan

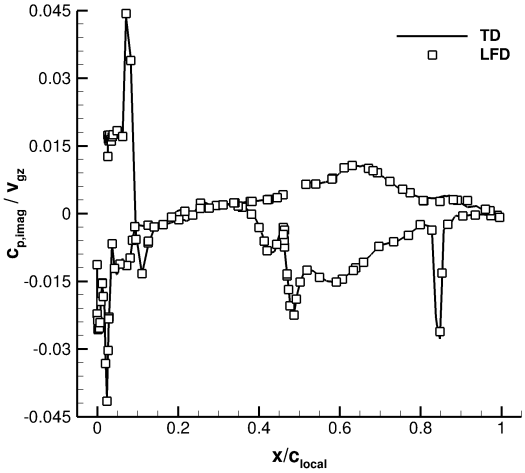

d) Imaginary part at 32% semi-wingspan

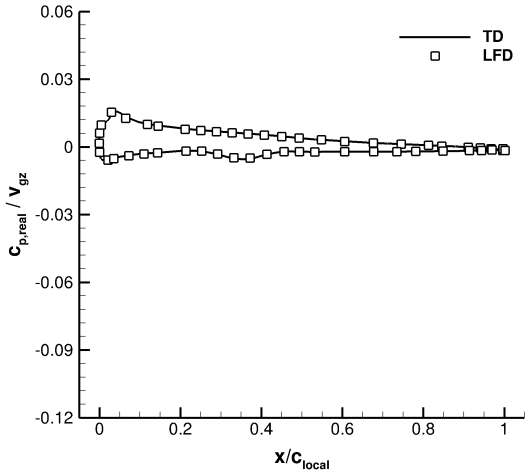

e) Real part at 75% semi-elevatorspan

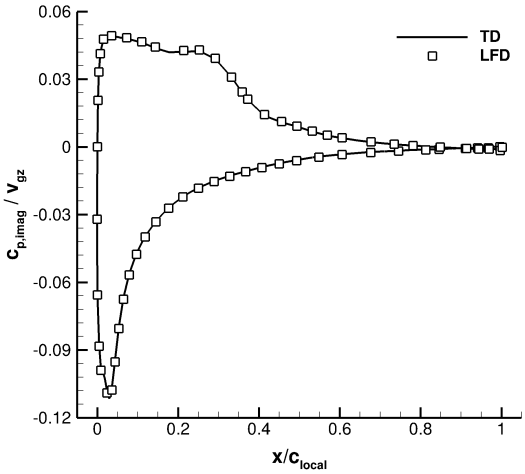

f) Imaginary part at 75% semi-elevatorspan

Figure 14. Sectional complex-valued pressure distributions for sinusoidal gust with $\omega^* = 0.073$

and imposing stricter unsteady convergence criteria, also these minor differences disappear. The second location at 32% semi-wingspan investigates surface pressures at the junction of wing, pylon and nacelle. Results for real and imaginary parts are displayed in Figs. 14c and 14d. Note that internal nacelle surfaces are ignored for visualisation purposes. Even in this challenging flow region results from both methods are in excellent agreement. The third slice is located at 75% semi-elevator span and results are presented in Figs. 14e and 14f. In comparison to previous sections on the wing no shock formation is present on the elevator, thus maximum values for real and imaginary part appear around the suction region with excellent agreement between time- and frequency-domain methods.

The frequency-domain gust response approach for the large civil aircraft is now used to investigate dynamic responses to realistic 1-cos gusts. **First, the influence of the chosen time-step size for all TD simulations is investigated for a 1-cos gust with $L_g = 116$ m. Whereas doubling the time-step size from its baseline value of 0.0015 s induces an error of 0.75% on the maximum lift coefficient, halving the time-step size results in a difference of 0.015%. Thus, the applied time-step offers a reasonable trade-off between computational time and achieved accuracy. Frequency-domain sampling data is produced at 15 reduced frequencies between 0 and 0.6 to cover the frequency range of interest for all gust lengths defined by the European Aviation Safety Agency in CS 25.341 [37]. Three gust lengths of $L_g = 18$, 116 and 214 m are analysed representing the shortest, longest and also a medium value. Amplitudes are chosen in accordance with the certification requirements and are in the order of 5% of the freestream velocity.**

The change in lift coefficient for all three gust lengths is shown in Fig. 15a. If the gust amplitude is set to 0.001% of the freestream velocity excellent agreement between a (then-linearised) time-domain simulation and LFD is obtained for $L_g = 214$ m once scaling the amplitude accordingly. Similar behaviour is expected for the other gust lengths. While nearly perfect agreement is also observed for the shortest gust length of $L_g = 18$ m, minor differences in the

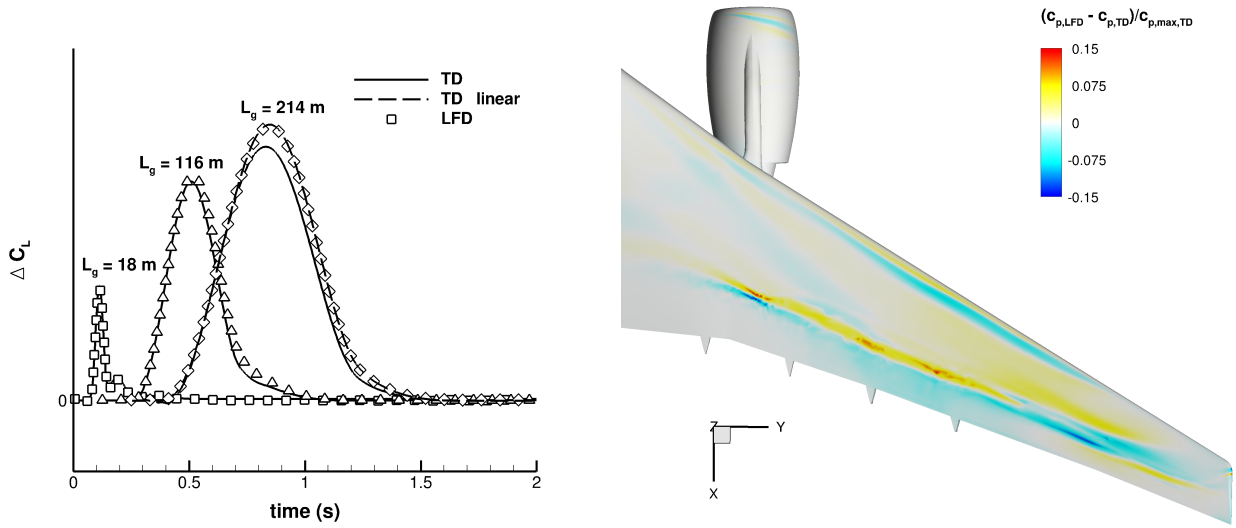

a) Lift coefficient history

b) Difference in surface pressure

Figure 15. History of lift coefficient following different 1-cos gusts and surface-pressure difference at peak load for $L_g = 116$ m

maximum lift coefficient as well as in the lift decay are observed for longer gusts. These discrepancies are caused by a dynamically non-linear response near the maximum lift coefficient during the time-marching simulation since an increasing gust length results in a larger gust amplitude due to the certification requirements [37]. The frequency-domain approach, however, assumes a dynamically linear response and is thus overpredicting the maximum lift coefficient. It should be noted that once dynamically non-linear phenomena are present the LFD method is, strictly speaking, no longer valid since the assumption of linear superposition is not fulfilled. Nevertheless, loads are conservatively predicted at several orders of magnitude reduced computational cost.

For $L_g = 116$ m the relative surface pressure difference at maximum lift coefficient is displayed in Fig. 15b showing values below 1% on the majority of the surface. Since a non-linear shock motion and a corresponding amplitude decrease occur during the time-domain analysis, the highest difference of around 10% arises close to the steady shock location. In addition, some minor discrepancies of 5% are present around the leading edge, caused by the same amplitude

Task	Cost
Time-domain simulation (single 1-cos response)	48.73 h
Frequency-domain sampling (15 frequencies)	9.78 h
a) Rebuilding global coefficients	0.01 h
b) Rebuilding surfaces pressure distributions	0.04 h

Table 4. Comparison of computational cost for aircraft case

mechanism.

Computational cost is presented for the two simulated approaches in Tab. 4. Timings were obtained on the UK based high power computing facility ARCHER[a] using 192 standard compute cores. Since the computational time for a TD 1-cos simulation depends on the investigated gust length, the time listed with 48.73 h is an average of all three gust responses. The time of 9.78 h covers the entire solution time for all 15 linear systems including the calculation of the right-hand side vector. Subsequent reconstruction of global coefficients and surface pressure distributions is negligible. Thus, the LFD method already offers a speed-up factor of roughly 5 compared to a single 1-cos time-marching response. As discussed in detail above, the frequency-domain solutions can be recycled to investigate an arbitrary time-domain signal, as long as the excited frequency range is covered. Unsteady time-marching simulations on the other hand need to be repeated for each change in gust parameter. Based on [38] a number of 20 different gust lengths at a given flight condition should be analysed during the certification process. Hence, the LFD approach offers a speed-up of two orders of magnitude compared to unsteady time-domain simulations for all gust lengths of interest, while still predicting loads conservatively.

V. Conclusion

A method is presented to efficiently compute the aerodynamic response of a rigid aircraft structure due to gust encounter. The Reynolds-averaged Navier–Stokes equations are first

[a]Advanced Research Computing High End Resource.

linearised around a non-linear steady-state solution, and resulting linear systems are then solved with an appropriate right-hand side to describe the gust excitation. Responses to various sinusoidal gusts are first computed to reconstruct an arbitrary gust encounter in the following, utilising a complex-valued superposition in conjunction with an incomplete inverse Fourier transform. In comparison with an unsteady time-marching approach computational cost is significantly reduced by two orders of magnitude when running a sufficient number of gust lengths.

Results are presented for a NACA0012 aerofoil at three different flow conditions, including sub- and transonic attached-flow cases and a post-buffet, detached-flow case. Excellent agreement compared with unsteady time-marching simulations is observed both for integrated aerodynamic coefficients and complex-valued surface pressures at various frequencies. The influence of the gust amplitude is visualised to analyse the assumption of a dynamically linear response around a non-linear steady state. Responses to 1-cos gusts are reconstructed from the individual sinusoidal responses with good agreement at all flow conditions.

A large civil aircraft is then analysed to build confidence in the method using a test case of industrial interest. Again, excellent agreement between the time- and frequency-domain results is achieved for complex-valued surface pressure distributions globally as well as in chosen wing and elevator sections. Responses to characteristic 1-cos gusts as defined by international certification authorities are reconstructed from sinusoidal responses and compared with corresponding non-linear time-marching simulations. Even for this complete aircraft configuration accurate predictions at two orders of magnitude cost reduction are demonstrated, thus showcasing the maturity of the linearised frequency-domain approach for industrial gust response simulations.

Besides analysing loads resulting from a dynamic response without structural deformation, the frequency-domain gust method offers the possibility to be used for dynamic loads analysis including structural responses. While a projection of surface forces onto structural eigenmodes is a well known approach, the construction of a reduced order model combining gust modes from proper

orthogonal decomposition and structural modes is an alternative.

Acknowledgements

The research leading to these results was co-funded by Innovate UK, the UK's innovation agency, as part of the Enhanced Fidelity Transonic Wing project. This work used the ARCHER UK National Supercomputing Service (http://www.archer.ac.uk).

References

[1] Albano, E. and Rodden, W. P., "A Doublet Lattice Method for Calculating Lift Distribution on Oscillating Surfaces in Subsonic Flow," *AIAA Journal*, Vol. 7, No. 2, 1969, pp. 279–285.

[2] Reimer, L., Ritter, M., Heinrich, R., and Krüger, W., "CFD-based Gust Load Analysis for a Free-flying Flexible Passenger Aircraft in Comparison to a DLM-based Approach," *22nd AIAA Computational Fluid Dynamics Conference*, 2015, AIAA Paper 2015-2455.

[3] Whitehead, D. S. and Grant, J. R., "Force and Moment Coefficients of High Deflection Cascades," *2nd International Symposium on Aeroelasticity in Turbomachinery*, 1981.

[4] Verdon, J. M. and Caspar, J. R., "Development of a Linear Unsteady Aerodynamic Analysis for Finite-Deflection Subsonic Cascades," *AIAA Journal*, Vol. 20, No. 9, 1982, pp. 1259–1267.

[5] Verdon, J. M. and Caspar, J. R., "A Linearized Unsteady Aerodynamic Analysis for Transonic Cascades," *Journal of Fluid Mechanics*, Vol. 149, 1984, pp. 403–429.

[6] Hall, K. C. and Clark, W. S., "Linearized Euler Predictions of Unsteady Aerodynamic Loads in Cascades," *AIAA Journal*, Vol. 31, No. 3, 1993, pp. 540–550.

[7] Hall, K. C., Clark, W. S., and Lorence, C. B., "A Linearized Euler Analysis of Unsteady Transonic Flows in Turbomachinery," *Journal of Turbomachinery*, Vol. 116, No. 3, 1994, pp. 477–488.

[8] Mortchéléwicz, G. D., "Application des Équations d'Euler Linéarisées á la Prévision du Flottement," *85th Meeting of the AGARD Structures and Materials Panel*, 1997, AGARD Report 822: Numerical Unsteady Aerodynamic and Aeroelastic Simulation.

[9] Widhalm, M., Dwight, R. P., Thormann, R., and Hübner, A. R., "Efficient Computation of Dynamic Stability Data with a Linearized Frequency Domain Solver," *5th European Conference on Computational Fluid Dynamics*, 2010, ECCOMAS CFD 2010.

[10] Weishäupl, C. and Laschka, B., "Small Disturbance Euler Simulations for Delta Wing Unsteady Flows due to Harmonic Oscillations," *Journal of Aircraft*, Vol. 41, No. 4, 2004, pp. 782–789.

[11] Clark, W. S. and Hall, K. C., "A Time-Linearized Navier-Stokes Analysis of Stall Flutter," *Journal of Turbomachinery*, Vol. 122, No. 3, 2000, pp. 467–476.

[12] Pechloff, A. and Laschka, B., "Small Disturbance Navier-Stokes Method: Efficient Tool for Predicting Unsteady Air Loads," *Journal of Aircraft*, Vol. 43, No. 1, 2006, pp. 17–29.

[13] Pechloff, A. and Laschka, B., "Small Disturbance Navier-Stokes Computations for Low-Aspect-Ratio Wing Pitching Oscillations," *Journal of Aircraft*, Vol. 47, No. 3, 2010, pp. 737–753.

[14] Thormann, R. and Widhalm, M., "Linear-Frequency-Domain Predictions of Dynamic-Response Data for Viscous Transonic Flows," *AIAA Journal*, Vol. 51, No. 11, 2013, pp. 2540–2557.

[15] Thormann, R. and Widhalm, M., "Forced Motion Simulation using a Linear Frequency Domain Solver for a Generic Transport Aircraft," *International Forum on Aeroelasticity and Structural Dynamics (IFASD)*, 2013, IFASD Paper 2013-17A.

[16] Kaiser, C., Thormann, R., Dimitrov, D., and Nitzsche, J., "Time-Linearized Analysis of Motion-Induced and Gust-Induced Airloads with the DLR TAU Code," *Deutscher Luft- und Raumfahrtkongress*, 2015.

[17] Förster, M. and Breitsamter, C., "Aeroelastic Prediction of Discrete Gust Loads Using Nonlinear and Time-Linearized CFD-Methods," *Journal of Aeroelasticity and Structural Dynamics*, Vol. 3, No. 3, 2015, pp. 252–255.

[18] Bekemeyer, P. and Timme, S., "Reduced Order Gust Response Simulation using Computational Fluid Dynamics," *57th AIAA/ASCE/AHS/ASC Structures, Structural Dynamics, and Materials Conference*, 2016, AIAA Paper 2016-1485.

[19] Thormann, R., Nitzsche, J., and Widhalm, M., "Time-linearized Simulation of Unsteady Transonic Flows with Shock-Induced Separation," *European Congress on Computational Methods in Applied Sciences and Engineering*, 2012, ECCOMAS 2012.

[20] Parameswaran, V. and Baeder, J. D., "Indicial Aerodynamics in Compressible Flow-Direct Computational Fluid Dynamic Calculations," *Journal of Aircraft*, Vol. 34, No. 1, 1997, pp. 131–133.

[21] Rodden, W. P., *Theoretical and Computational Aeroelasticity*, Crest Publishing, 1st ed., 2011.

[22] Seidel, D., Bennett, R., and Whitlow, J. R., "An exploratory study of finite difference grids for transonic unsteady aerodynamics," *21st Aerospace Sciences Meeting*, 1983, AIAA Paper 1983-0503.

[23] Thormann, R. and Timme, S., "Efficient Aerodynamic Derivative Calculation in Three-Dimensional Transonic Flow," *Royal Aeronautical Society - Applied Aerodynamics Conference*, 2016, AAC paper R1.

[24] Schwamborn, D., Gerhold, T., and Heinrich, R., "The DLR TAU-Code: Recent Applications in Research and Industry," *European Conference on Computational Fluid Dynamics*, 2006, ECCOMAS CFD 2006.

[25] Spalart, P. R. and Allmaras, S. R., "A One-Equation Turbulence Model for Aerodynamic Flows," *Recherche Aerospatiale*, Vol. 1, 1994, pp. 5–21.

[26] Jameson, A., Schmidt, W., and Turkel, E., "Numerical Solutions of the Euler Equations by Finite Volume Methods Using Runge-Kutta Time-Stepping Schemes," *14th Fluid and Plasma Dynamic Conference*, 1981, AIAA Paper 1981–1259.

[27] Dwight, R., "An Implicit LU-SGS Scheme for Finite-Volume Discretizations of the Navier-Stokes Equations on Hybrid Grids," *DLR-FB-2005-05*, 2006.

[28] Xu, S., Timme, S., and Badcock, K. J., "Enabling off-design linearised aerodynamics analysis using Krylov subspace recycling technique," *Computers and Fluids*, Vol. 140, 2016, pp. 385–396.

[29] Saad, Y., *Iterative Methods for Sparse Linear Systems*, Society for Industrial and Applied Mathematics, Philadelphia, PA, 2nd ed., 2003.

[30] Stickan, B., Dillinger, J., and Schewe, G., "Computational aeroelastic investigation of a transonic limit-cycle-oscillation experiment at a transport aircraft wing model," *Journal of Fluids and Structures*, Vol. 49, No. August 2014, 2014, pp. 223–241.

[31] Neumann, J. and Mai, H., "Gust response: Simulation of an Aeroelastic Experiment by a Fluid-Structure Interaction Method," *Journal of Fluids and Structures*, Vol. 38, 2013, pp. 290–302.

[32] Nitzsche, J., "A Numerical Study on Aerodynamic Resonance in Transonic Separated Flow," *International Forum on Aeroelasticity and Structural Dynamics (IFASD)*, 2009, IFASD Paper 2009-126.

[33] Iovnovich, M. and Raveh, D. E., "Transonic Unsteady Aerodynamics in the Vicinity of Shock-Buffet Instability," *Journal of Fluids and Structures*, Vol. 29, 2012, pp. 131–142.

[34] Timme, S. and Thormann, R., "Towards Three-Dimensional Global Stability Analysis of Transonic Shock Buffet," *16th AIAA Aviation Technology*, 2016, AIAA Paper 2016-3848.

[35] Broyden, C. G., "A class of methods for solving nonlinear simultaneous equations," *Mathematics of Computation (American Mathematical Society)*, Vol. 19, No. 92, 1965, pp. 577–593.

[36] Michler, A., "Aircraft control surface deflection using RBF-based mesh deformation," *International Journal for Numerical Methods in Engineering*, Vol. 88, 2011, pp. 986–1007.

[37] European Aviation Safety Agency, "Certification Specifications for Large Aeroplanes (CS-25)," 2015.

[38] European Aviation Safety Agency, "Certification Specifications for Large Aeroplanes Amendment 17 (CS-25)," 2015.